Numerical simulations of the flow around a spinning projectile in subsonic regime

Javier Garibaldi ⊗ , Mario Storti ‡ , Laura Battaglia ‡ and Jorge D'Elía ‡

⊗Instituto de Investigaciones Científicas y Técnicas de las Fuerzas Armadas (CITEFA)

San Juan Bautista de La Salle 4397 (B1603ALO) Villa Martelli, ARGENTINA

ph.: (5411)-4709 8100, fx: (5411)-4709 8228

e-mail: jgaribaldi@citefa.gov.ar, web page: http://www.citefa.gov.ar

‡Centro Internacional de Métodos Computacionales en Ingeniería (CIMEC)

Instituto de Desarrollo Tecnológico para la Industria Química (INTEC)

Universidad Nacional del Litoral - CONICET

Güemes 3450, 3000-Santa Fe, ARGENTINA

ph.: (54342)-4511 594/5, fx: (54342)-4511 169

e-mail: (mstorti, jdelia)@intec.unl.edu.ar, lbattaglia@ceride.gov.ar

web page: http://www.cimec.org.ar

August 21, 2007

Key Words: spinning projectile model, incompressible subsonic flow, large eddy simulation (LES), finite element method, large scale and distributed computing, fluid mechanics.

Abstract

The unsteady flow around a 155 mm projectile governed by the Navier-Stokes (NS) equations is numerically solved with a Large Eddy Simulation (LES) scheme, together with the Sub-Grid Scale (SGS) solved by a Smagorinsky model and the van Driest near-wall damping. The computed results are obtained in the subsonic flow regime for a viscous and incompressible Newtonian fluid in order to determine the axial drag coefficient, and they are validated against experimental data. The problem was solved by a monolithic finite element code for parallel computing on a Beowulf cluster.

1 Introduction

There are two main factors to distinguish projectile aerodynamics from classic aerodynamics. The first one is the fact that most projectiles have an axis or plane of symmetry, which implies also symmetric aerodynamic parameters. The second one is related to large spinning velocities that, for tube artillery, are from $5,000$ to $10,000$ Revolutions Per Minute (RPM), generating aerodynamic effects which are present only in the aeroballistic area. Among these particular parameters, there are the force and the torque produced by the Magnus effect. Although this force is relatively lower than the lift and can be ignored, the torque is critical for the projectile stability [1].

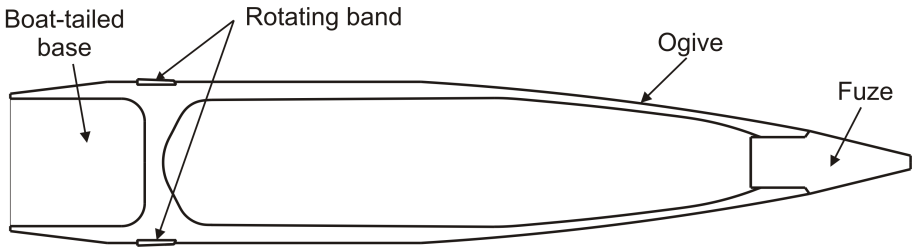

Figure 1: Relevant projectile parts.

In general, a conventional artillery spinning projectile counts on a central cylindrical body to be guided through the cannon tube, and a frontal ogive whose length measures from one and a half to three times the caliber, see Fig. 1, resulting in a configuration with a drag higher than other flying corps, and where the drag force is mostly due to the pressure. It is important to notice that this geometry places the pressure center ahead of the gravity center, see Fig. 2, that would make the projectile overturn if it were not stabilized. The mechanism used for avoiding the overturn is the spinning, i.e. the projectile is launched with an appropriate rotational velocity given around its longitudinal axis. This rotational velocity is generated during the travel of the object through the cannon tube due to the interaction between the rotating band and the rifling inside the cannon tube. Under the conditions described, any destabilizing torque over the projectile makes it react with a rotation over a plane normal to the torque plane, originating nutation and precession. The first of them is quickly damped, whereas the second holds during the rest of the trajectory, but it is theoretically restricted by design to 5° or less around the translational direction.

The flow around a projectile presents turbulent boundary layers, whose separation is a usual phenomena, and a large turbulent wake formed at the bottom of the object. In ballistic aerodynamics, prevention or control of the separation of the boundary layer is one of the most important aims, as

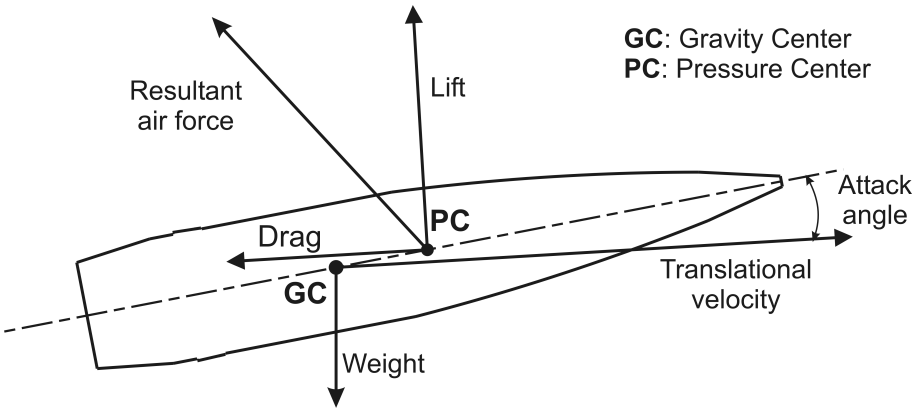

Figure 2: Sketch of aerodynamic forces acting on a projectile.

well as an appropriate ogive design. Typical velocities for field artillery projectiles are from 150 m/s to 900 m/s or even more, reaching subsonic, transonic or supersonic flow regimes around them. Then, a complete characterization should consider analysis tools appropriate for each of them, as those employed in [2] and [3].

As it is well known, a turbulent flow carries irregular and fluctuating fluid motions which contribute significantly to the transport phenomena. They are always three-dimensional, unsteady and mainly irregular except perhaps by coherent structures, which are as some kind of organized flow motion that can be recognized in the instantaneous flow fields as well as in the time-averaged ones [4]. There are also eddies with a wide spectrum of sizes, from the larger ones close to the flow domain ones, to the much smaller ones at which viscous dissipation takes place. The numerical techniques available in Computational Fluid Dynamics to simulate them can be split in three main types [5, 6]:

i) Direct Numerical Simulation (DNS): where a numerical method solves the three-dimensional Navier-Stokes and continuity equations (the NS system for brevity) for all scales and without any extra model for the smallest ones, so the mesh size step must be smaller than the small-length scales. As the relation of this to the large-length scales varies inversely with the Reynolds (Re) number and the computation have to be always three-dimensional, the number of grid points and computational cost increases roughly with the third power of the Re number, i.e., scale as $O(\mathrm{Re}^3)$. Then, a DNS alternative results expensive for numerical studies in engineering applications considering that most of the computational effort is put over the smaller scales, which are not the important from the point of view of determining global flow values as forces over the projectile.

ii) Large Eddy Simulation (LES): is less expensive than DNS so it can be used in engineering cases where large-scale sizes dominate the flow behavior and steadiness prevails. Besides, according to [7], LES generally converges to DNS as the spatial and temporal steps decrease. Strictly, the simulation is always three-dimensional and unsteady, where only the scale-motions greater than the mesh size are obtained by solving the unsteady Navier-Stokes system while the scale-motions smaller that the mesh size are accounted by some pair of subgrid and near-wall models. A near-wall model is more relevant than the subgrid one for high Reynolds number flows since the length-scales decrease with the increment of the Re number, in particula, the number of grid points needed to a good resolution of the near-wall zones increases roughly with the square of the Re number, i.e. scale as $O(\mathrm{Re}^2)$.

iii) Reynolds-Averaged Navier-Stokes (RANS): where a model to account the whole spectrum of length scales is necessary as all turbulent fluctuations are averaged out from the equations to be solved. Even when RANS methods count on many models for solving the Reynolds stresses which are necessary for the closure of the problem, see [8], it is not easy to find the most appropriate, especially in the detached flow regions, and they are not capable to deal with massively separated flows characterized by large-scale structures, or coherent ones, which are determinant for the estimation of aerodynamic forces.

A LES model is chosen since the Re number range to be considered indicates that the flow is fully turbulent. Its adoption responds mainly to the computed large-scales, associated to the coherent structures developed due to the projectile motion. As already stated, the smaller scales are not solved but they are modeled, regarding that its influence over the other scales is related to energy transfers [9].

There is a considerable experience about the use of computational methods for solving flow problems around projectiles, most of them supported by validation against experimental results, for instance, in exterior [10, 11] and interior [12] flow ballistics.

The projectile studied here is the PACU one (Proyectil Argentino de CUlote hueco), a 155 mm caliber shell designed by CITEFA and used now a days by the Argentinian Army. The aerodynamic study, which includes the spinning effects and the simulation of the turbulent flow regime with boundary layer separation is made by the PETSc-FEM code [13, 14], which is a parallel multiphysics finite element program based on the Message Passing Interface (MPI) [15] and the Portable Extensible

Toolkit for Scientific Computations (PETSc) [16, 17]. Once the computer results are obtained, a comparison is made to experimental data obtained by analyzing the shell velocity evolution registered by Doppler radar measurements, as is extensively considered in [18].

2 Stabilized finite elements by a SUPG-PSPG method

In this section, specific characteristics about the finite element method (FEM) selected for solving the problem are given, such as the discretized equations and the finite elements kind itself, as well as the parallel implementation.

2.1 Navier-Stokes equations

The Navier-Stokes equations for a viscous and incompressible fluid flow are written as

$$\nabla \cdot \boldsymbol{u} = 0 \; ; \tag{1}$$

$$\rho \left(\partial_t \boldsymbol{u} + \boldsymbol{u} \cdot \nabla \boldsymbol{u} \right) = \nabla \cdot \boldsymbol{\sigma} + \boldsymbol{f} \; ; \tag{2}$$

in $\Omega \times [0, T]$. The position vector $\boldsymbol{x} = (x, y, z)$ is related to an Eulerian reference system, t is the time variable, Ω is the flow region, $[0, T]$ is some time interval, $\boldsymbol{u} = (u_x, u_y, u_z)$ and ρ are the velocity and density, respectively, with $\boldsymbol{f}$ the vector of external forces. The fluid stress tensor $\boldsymbol{\sigma}$ is decomposed into its isotropic $-p\boldsymbol{I}$ and deviatoric $\boldsymbol{T}$ parts

$$\boldsymbol{\sigma} = -p\boldsymbol{I} + \boldsymbol{T} \; ; \tag{3}$$

where p is the pressure and $\boldsymbol{I}$ is the identity tensor. As only Newtonian fluids with constant physical properties are considered, its deviatoric part $\boldsymbol{T}$ is related linearly to the strain rate tensor $\boldsymbol{\epsilon}(\boldsymbol{u})$ with

$$\boldsymbol{T} = 2\mu\boldsymbol{\epsilon} \quad ; \quad \boldsymbol{\epsilon} = \frac{1}{2}\left[\nabla \boldsymbol{u} + (\nabla \boldsymbol{u})^T\right] \; ; \tag{4}$$

where μ is the dynamic viscosity of the fluid and $(...)^T$ denotes the transpose. Dirichlet, Neumann and wall law boundary conditions are taken into account, respectively,

$$\begin{aligned} \boldsymbol{u} &= \boldsymbol{g} && \text{on } \Gamma_g; \\ \boldsymbol{n} \cdot \boldsymbol{\sigma} &= \boldsymbol{h} && \text{on } \Gamma_h; \\ \boldsymbol{n} \cdot \boldsymbol{\sigma} &= \boldsymbol{h}_{\text{wall}}(\boldsymbol{u}) && \text{on } \Gamma_{\text{wall}}; \end{aligned} \tag{5}$$

and the initial condition is a specified divergence-free velocity field $\boldsymbol{u}(\boldsymbol{x}, 0) = \boldsymbol{u}_0$ on the flow domain Ω.

2.2 The SUPG-PSPG formulation

The incompressible NS equations in the incompressible case present two important difficulties for the solution with finite elements. First, the character of these equations become highly advective dominant when the Re number increases. In addition, the incompressibility condition represents a constraint on the system. This has the drawback that only some combinations of interpolation spaces for velocity and pressure fields can be used with the Galerkin formulation, namely those that satisfy the so-called Ladyzhenskaya-Brezzi-Babuska condition. The advection and the incompressibility equations are stabilized with the Streamline Upwind Petrov Galerkin (SUPG) [19, 20] and the Pressure Stabilizing Petrov Galerkin (PSPG) [21, 22] stabilization terms, respectively. In this way, it is possible to use stable equal order interpolations. To enforce the satisfaction of the discrete continuity equation, an extra stabilization term is added, called Least Square Incompressibility Constraint (LSIC). The flow domain Ω is partitioned in E finite elements Ω_e, with $e = 1, 2, \ldots, E$, while the interpolation spaces and weighting functions are:

$$\begin{aligned}
\mathcal{U}_{\boldsymbol{u}}^h &= \left\{ \boldsymbol{u}^h \text{ such that } \boldsymbol{u}^h \in H_d^h \text{ and } \boldsymbol{u}^h\big|_{\Gamma_g} = \boldsymbol{g}^h \right\} \\
\mathcal{P}_q^h &= \left\{ q^h \text{ such that } q^h \in H_1^h, \text{ with } \textstyle\int_\Omega q^h d\Omega = 0 \text{ and } q^h\big|_{\Gamma_h} = 0 \right\} \\
\mathcal{W}_{\boldsymbol{u}}^h &= \left\{ \boldsymbol{w}^h \text{ such that } \boldsymbol{w}^h \in H_d^h \text{ and } \boldsymbol{w}^h\big|_{\Gamma_g} = 0 \right\}
\end{aligned} \tag{6}$$

with $H_d^h = \left(H_1^h\right)^d$, where d is the number of space dimensions and the Sobolev space

$$H_1^h = \left\{ \phi^h \text{ such that } \phi^h \in C^0(\overline{\Omega}) \text{ and } \phi^h|_{\Omega^e} \in \mathcal{L}^1 \right\} \ ; \tag{7}$$

for all $\Omega^e \in \mathcal{E}$, where $\mathcal{L}^1$ is the set of polynomials of first order while $\mathcal{E}$ is the set of elements. The combined SUPG/PSPG formulation for Eqs. (1-2) can be written as: *find* $\boldsymbol{u}^h \in \mathcal{U}_u^h$ *and* $p^h \in \mathcal{P}_q^h$

such that:

$$\begin{aligned}
&\int_\Omega \boldsymbol{w}^h \cdot \rho\Big(\partial_t \boldsymbol{u}^h + \boldsymbol{u}^h \cdot \nabla \boldsymbol{u}^h\Big) d\Omega + \int_\Omega \boldsymbol{\epsilon}(\boldsymbol{w}^h) : \boldsymbol{\sigma}^h d\Omega \; + \\
&+ \underbrace{\sum_{e=1}^{E} \int_{\Omega^e} \boldsymbol{\delta}^h \cdot \Big[\rho\left(\partial_t \boldsymbol{u}^h + \boldsymbol{u}^h \cdot \nabla \boldsymbol{u}^h\right) - \nabla \cdot \boldsymbol{\sigma}^h\Big] d\Omega}_{\text{(SUPG)}} \; + \\
&+ \underbrace{\sum_{e=1}^{E} \int_{\Omega^e} \boldsymbol{\epsilon}^h \cdot \Big[\rho(\partial_t \boldsymbol{u}^h + \boldsymbol{u}^h \cdot \nabla \boldsymbol{u}^h) - \nabla \cdot \boldsymbol{\sigma}^h\Big] d\Omega}_{\text{(PSPG)}} \; + \\
&+ \sum_{e=1}^{E} \int_{\Omega^e} \nu_{\text{LSIC}} \nabla \cdot \boldsymbol{w}^h \rho \nabla \cdot \boldsymbol{u}^h d\Omega + \int_\Omega q^h \nabla \cdot \boldsymbol{u}^h d\Omega = 0 \; ;
\end{aligned} \tag{8}$$

for all $\boldsymbol{w}^h \in \mathcal{W}_u^h$ *and* $q^h \in \mathcal{P}_q^h$. In Eq. (8) three stabilization terms are added to the standard Galerkin formulation: the parameter $\boldsymbol{\delta}^h$ corresponds to the SUPG stabilization, the $\boldsymbol{\epsilon}^h$ parameter corresponds to the PSPG one, and finally the ν_{LSIC} parameter to enforce the incompressibility constraint. The first two terms are defined over different functional spaces and they can be written as $\boldsymbol{\delta}^h = \tau_{\text{SUPG}}\ (\boldsymbol{u}^h \cdot \nabla)\boldsymbol{w}^h$ and $\boldsymbol{\epsilon}^h = \tau_{\text{PSPG}}\ \rho^{-1} \nabla q^h$, where

$$\begin{aligned}
\tau_{\text{SUPG}} &= \frac{h_{\text{e}}}{2||\boldsymbol{u}^h||} z(\text{Re}_{\text{u}^\text{h}}) \; ; \\
\tau_{\text{PSPG}} &= \frac{h_{\text{e}}^*}{2||\boldsymbol{U}||} z(\text{Re}_{\text{U}}^*) \; ; \\
\nu_{\text{LSIC}} &= \frac{h_{\text{e}}^*}{2} ||\boldsymbol{u}^h||\ z(\text{Re}_{\text{u}^\text{h}}) \; ;
\end{aligned} \tag{9}$$

while $\text{Re}_{\text{u}^\text{h}}$ and Re_{U}^* are the Reynolds number based on the element velocity $\boldsymbol{u}^h$ and a global characteristic velocity $\boldsymbol{U}$, respectively, that is,

$$\text{Re}_{\text{u}^\text{h}} = \frac{||\boldsymbol{u}^\text{h}||\ \text{h}_\text{e}}{2\nu} \quad \text{and} \quad \text{Re}_{\text{U}}^* = \frac{||\boldsymbol{U}||\ \text{h}_\text{e}^*}{2\nu} \; . \tag{10}$$

The element size h_e is computed as

$$h_\text{e} = 2 \left[\sum_{a=1}^{n_e} |\boldsymbol{s} \cdot \nabla w_a| \right]^{-1} \; ; \tag{11}$$

where w_a is the function associated to node a, n_e is the number of nodes connected to the element and $\boldsymbol{s}$ is the streamline oriented unit vector, while the element size h_e^* is defined as the diameter of the sphere with the same element volume. Finally, the function $z(\text{Re})$ in Eqs. (9) is defined as

$$z(\text{Re}) = \begin{cases} \text{Re}/3 & 0 \leq \text{Re} < 3 \; ; \\ 1 & 3 \leq \text{Re} \; . \end{cases} \tag{12}$$

2.3 Large Eddy Simulation

In LES techniques, the momentum balance equations are solved with an "effective" kinematic viscosity $\nu_e = \nu + \nu_t$, which is the sum of the molecular part calculated as $\nu = \mu/\rho$, plus a "turbulent" one ν_t. The last one is estimated in the PETSc-FEM [13] code by means of the Smagorinsky [23] sub-grid model coupled with the van Driest near-wall damping factor f_ν, and given by

$$\begin{aligned} \nu_t &= C_S^2 h_e^2 f_\nu \sqrt{\boldsymbol{\epsilon}(\boldsymbol{u}) : \boldsymbol{\epsilon}(\boldsymbol{u})} \ ; \\ f_\nu &= 1 - \exp\left(-y^+/A^+\right) \ ; \end{aligned} \tag{13}$$

in which C_S is the Smagorinsky constant ($C_S \approx 0.10$ for flows in ducts) and $\sqrt{\boldsymbol{\epsilon}(\boldsymbol{u}) : \boldsymbol{\epsilon}(\boldsymbol{u})}$ is the trace of the strain rate $\boldsymbol{\epsilon}(\boldsymbol{u})$. The van Driest near-wall damping factor f_ν reduces the "turbulent" kinematic viscosity close to the solid walls, but it introduces a no-local effect in the sense that the "turbulent" kinematic viscosity ν_t at a volume element also depends on the state of the fluid at the closest wall. A constant value $A^+ = 25$ is adopted, while $y^+ = y/y_w$ is the non-dimensional distance from the nearest wall expressed in wall units $y_w = \nu/u_\tau$, where $u_\tau = (\tau_w/\rho)^{1/2}$ is the local friction speed and τ_w is the local wall shear stress.

2.4 Parallel computing

The numerical simulations were performed using a domain decomposition technique [24] in the PETSc-FEM [13] code, which is a parallel multiphysics finite element library [25, 26, 27] based on the Message Passing Interface (MPI) [15] and the Portable Extensible Toolkit for Scientific Computations (PETSc) [16]. The problem was solved using the Beowulf cluster "Geronimo" [28, 29], with 11 nodes P4 with 2 GBytes of RAM memory each. Other authors also appeal to parallel computations for solving similar problems, see [10, 11].

3 Experimental results

In Exterior Ballistics, the specialty related to projectile flight studies, the drag coefficient curves take a fundamental role for different applications, such as the generation of firing tables. These curves can be obtained also from tests inside wind tunnels or theoretical calculus. In the first case, the interferences between the projectile or its model and the tunnel walls affects the precision of results; in the second, the hypothesis adopted could move the results away from the real behavior.

Because of the limitations of the methods mentioned before, a different way for the making up of these curves is the identification of the aerodynamic properties of an object from flight tests over a real specimen. One of these techniques is the obtaining of drag curves from data registered by a Doppler radar, as it was made in this case. For this work, there were two devices: a TERMA DR-5000 trajectory analyzer, and also a rawinsonde Marwin MW12, which provides information to the radar about atmospheric conditions during the test flight.

The flight velocity data measured by the radar are used for determining the drag coefficient, called here C_D. Notice that this coefficient does not correspond to a non-null attack angle nor a null one because this angle is an unknown under experimental conditions. Then, the C_D calculated by the Doppler radar reflects the combined effects of the lift and drag induced by the gyroscopic angular movement of the projectile around its mass center.

The trajectory model used by the radar counts on three degrees of freedom, the same as in the widely used Point Mass Trajectory Model (PMTM) which is a model that allows the estimation of the trajectory and the impact points of projectiles. A more complete one is the Modified Point Mass Trajectory Model (MPMTM), that is applied when there are more aerodynamic coefficients available than in the other method. Both of the methods are introduced in [30].

Besides, a drag coefficient curve of an artillery projectile can be determined from radar measured velocity data obtained from flight tests through the *Optimal Dynamic Fitting Method*. A complete discussion about this subject can be found in [31].

Some shooting tests were carried out with PACU projectiles in proving grounds, under the scope of the CITEFA test projects and with the assistance of the equipment mentioned before, composed by a radar and a rawinsonde, where for the subsonic regime the drag coefficient estimated according to the measurements is $C_D \approx 0.130$.

4 Geometric and numerical model

The geometry of the projectile was modeled by a computer assisted design (CAD) system, see Fig. 3, and then was inserted in a cylindrical cavity which conforms the whole domain of calculus, resembling a wind tunnel, as can be seen also in Fig. 3.

The generation of an appropriate finite element mesh demanded more time than the expected one during the pre-processing stage because of the geometric definition of the model, and later for

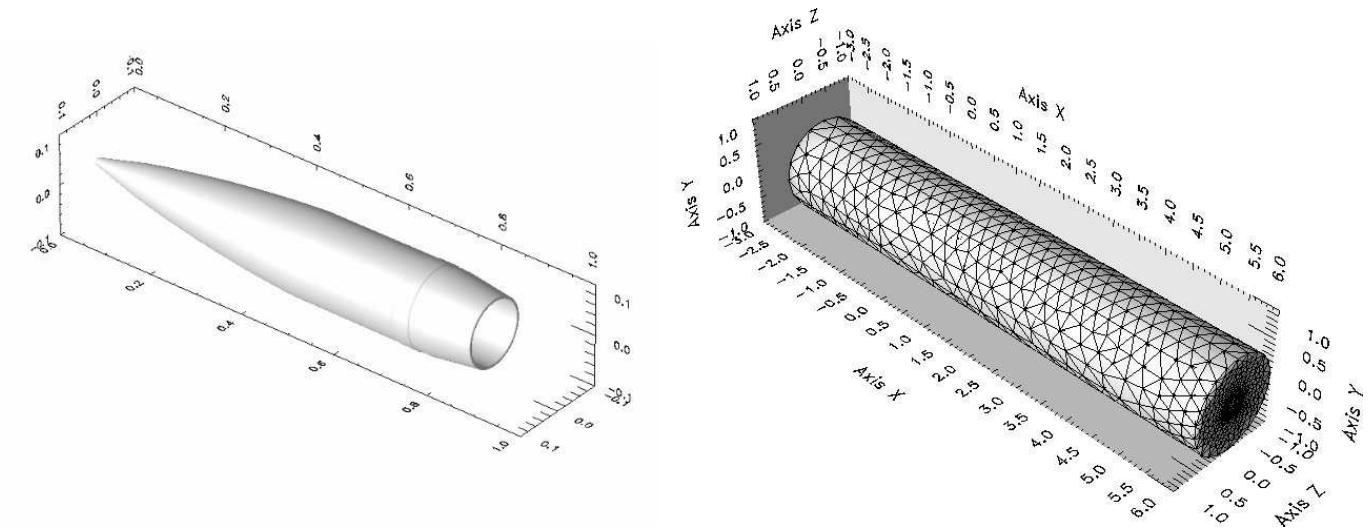

Figure 3: Main dimensions of the projectile model (left) and meshed domain (right).

the quality of the finite elements obtained. The mesh finally used for calculation, see Fig. 4, was generated by a mesher developed in CIMEC [32] and it counts on 756 k-elements of linear tetrahedral type and 159 k-nodes, approximately, where the space behind and around the projectile was carefully discretized considering the boundary layer, the wake and their influence over the results.

The data used were established based on the knowledge about artillery ordnance in CITEFA. From this point of view, the typical attack angle of an artillery projectile during a correctly stabilized flight and for a low-curvature trajectory is between 0° and 3°, as appreciated in the experimental tests. Higher attack angles are registered for trajectories with more curvature, as in the case of maximum reach, where the angles may take values of 5° or more in the apex. On the other hand, the translational velocities usually registered in subsonic flights are around 100 m/s when projection charges are of low velocity and short reach, whereas the rotational velocity is imposed by the rifling inside the cannon tube, as said before.

Regarding that, computational simulations over the projectile were performed for a translational velocity of 100 m/s, a spin velocity of 5200 RPM, and the kinematic viscosity of air of $\nu = 1.5 \times 10^{-5}$ m^2/s. These parameters allows the estimation of the Reynolds number, which takes values of order 1×10^7, indicating that the flow is turbulent and a turbulence model is needed for solving the problem. Besides, the flow is considered incompressible because the Mach number is $M \approx 0.3$, indicating that the flow is subsonic.

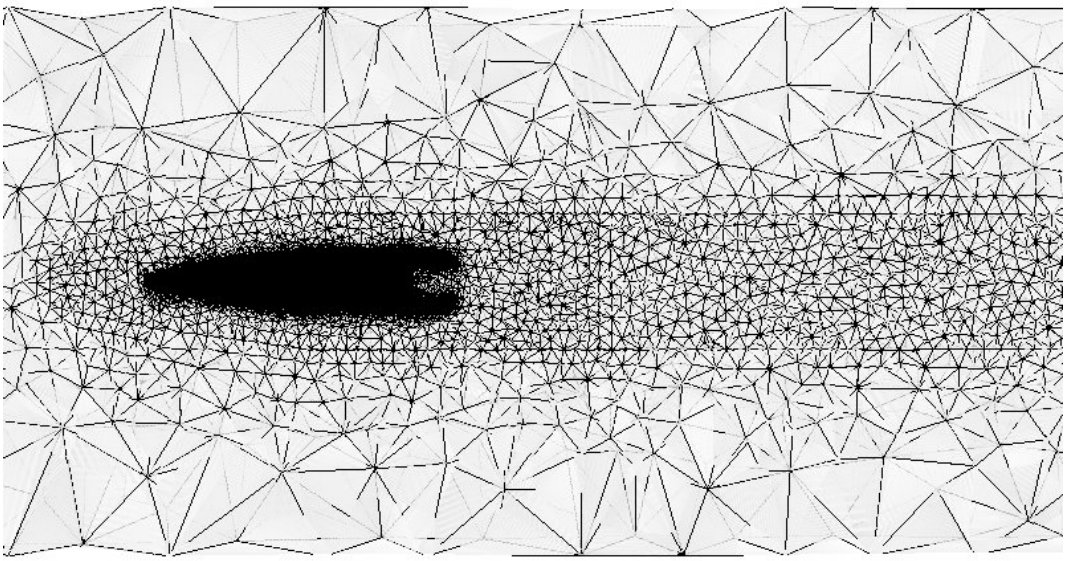

Figure 4: Section of the domain of analysis, where mesh refinement can be appreciated in the wake and around the projectile.

5 Numerical results

The calculations include the cases with attack angles of 0° and 5°, being all of these conditions appropriate for comparing the numerical results with the experimental ones.

The streamlines for null attack angle are shown in Fig. 5, where it can be seen that those originated closer to the object show a rotational effect. The vorticity over the projectile surface for the attack angles 0° and 5° are shown Fig. 6. In Fig. 7, the absolute velocity around the projectile is showed over a vertical plane for 0° of attack angle, while the static pressure around the projectile and over the wake and the numerical drag coefficients for the same case are presented in Figs. 8 and 9, respectively. Integration over the pressures registered over the projectile surface gave the net force exerted by the air over the object. These calculations are translated later to the drag coefficients in the three directions, CD_x, CD_z ans CD_y, which in the case of 5° take the mean corresponding values of 0.150, 0.098 and 0.430, see Fig. 10.

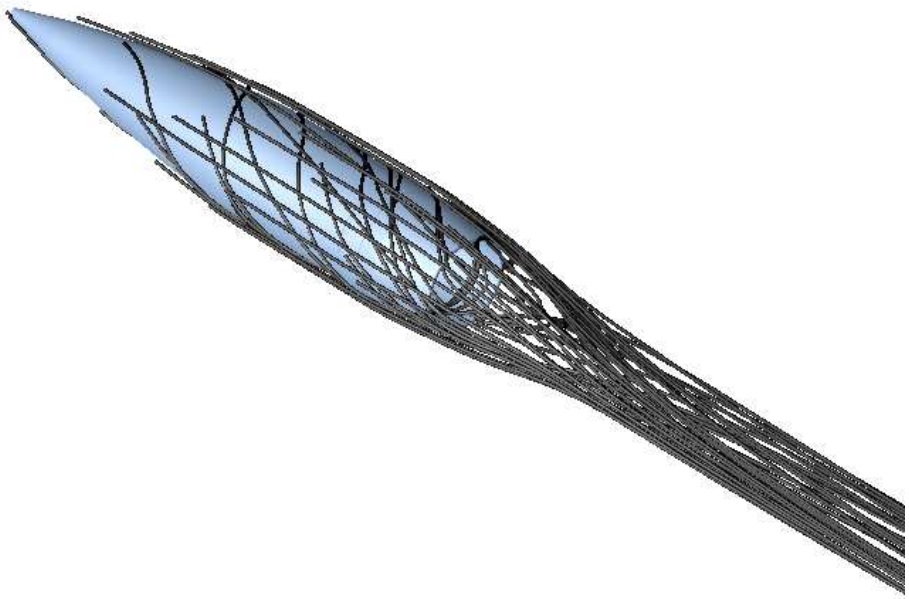

Figure 5: Streamlines for null attack angle. Those originated closer to the object show the rotational effect.

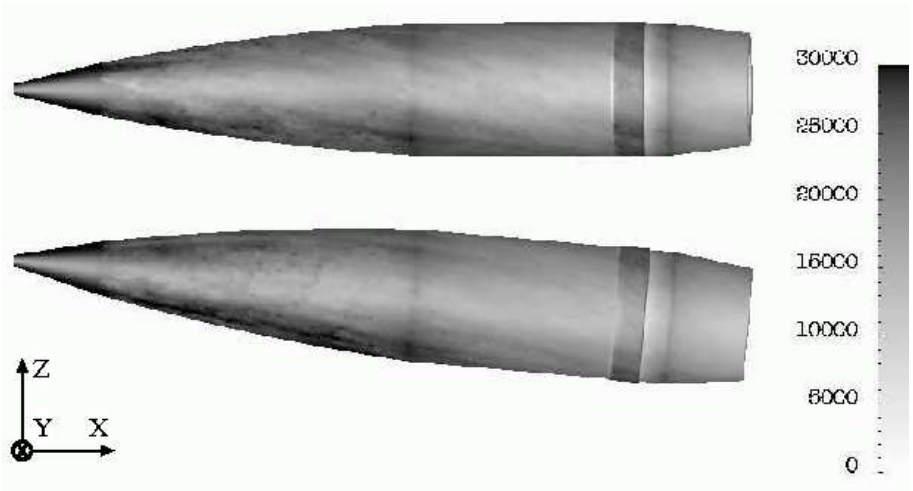

Figure 6: Vorticity over the projectile surface for the attack angles considered, 0° and 5°.

6 Discussion

Comparing the drag coefficient curves obtained by the numerical simulations for 0° (Fig. 9) and 5° (Fig. 10), it is possible to see that in the second one there is a much higher lift in z direction and a more important lateral drag component in y direction due to the Magnus effect. The explanation is

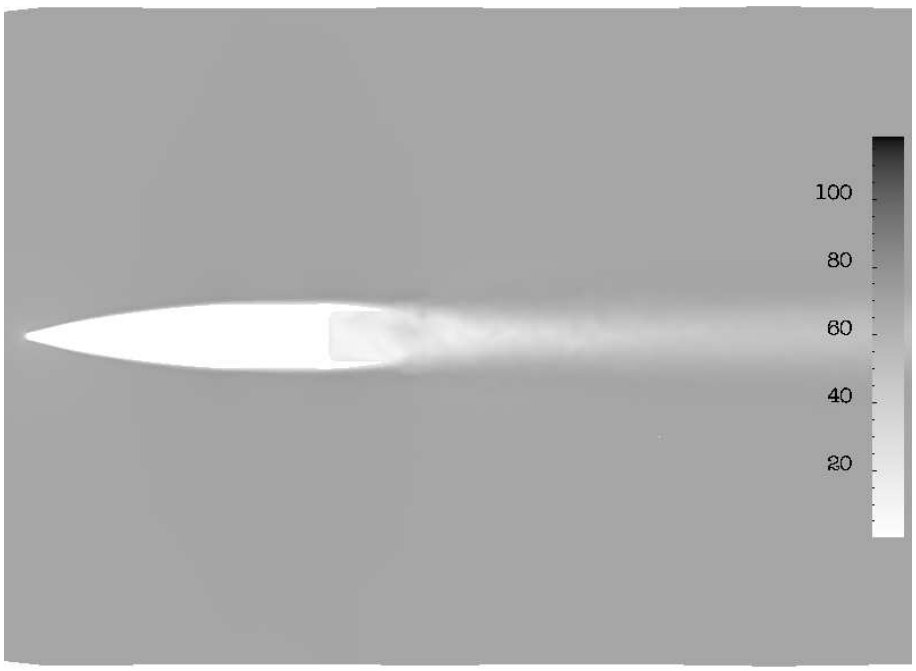

Figure 7: Absolute velocity around the projectile, showed over a vertical plane for 0° of attack angle.

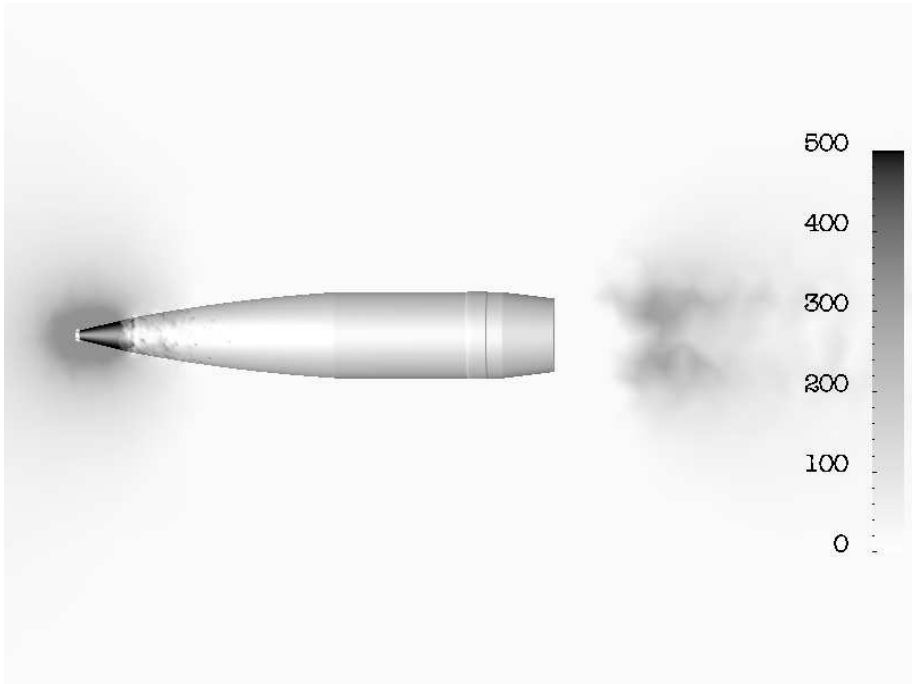

Figure 8: Static pressure around the projectile and over the wake. Angle of attack of 0°.

that the inclined projectile, which is spinning clockwise if it is seen from front, receives more wind underneath that produces a force which pushes it to left, i.e., to the $+y$ axis, besides the important increment in z direction.

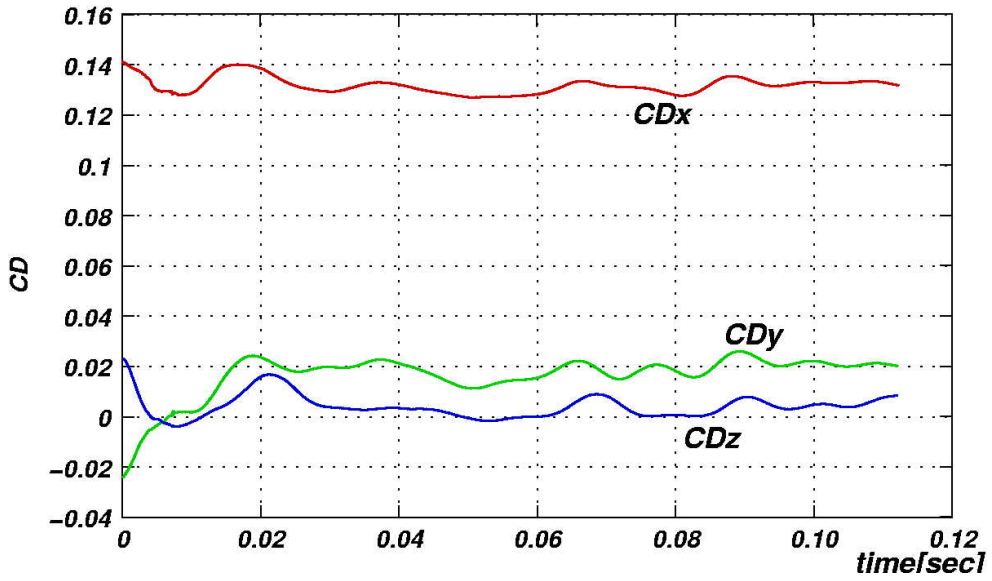

Figure 9: Drag coefficients determined numerically for null attack angle.

Some comments arise after considering both the experimental and the numerical results, and they are summarized in the following paragraphs.

One of the most important issues is that the drag coefficient predicted by the PETSc-FEM code for an attack angle of 0° is $C_D^{\text{num}}(0°) = 0.132$, which has very good agreement with the one obtained experimentally, $C_D^{\text{exp}}(0°) = 0.130$. Although the numerical calculations does not take into account the precession movement that is certainly present in shooting tests, this difference does not invalidate the computational analysis as a good first approximation. Besides, a correctly stabilized projectile over an almost rectilinear trajectory does not show attack angles higher than 3°.

The elaboration of a series of analogous numerical studies to be solved with PETSc-FEM involving velocities of 100 to 200 m/s and attack angles from 0° to 5° would give an even better characterization of the subsonic projectile flight.

As mentioned in Sec. 3, there are trajectory methods for determining the impact points of the shell. Among them, the already mentioned MPMTM is able to predict the whole flight trajectory of a projectile and even the drift, i.e., the displacement of the object outside of the shooting plane. By applying this method, it could be possible to make another verifications, taking the drag, lift and Magnus coefficients from the numerical analysis, and making a comparison with the impact points experimentally determined by CITEFA with a Global Positioning System (GPS) in the artillery proving ground.

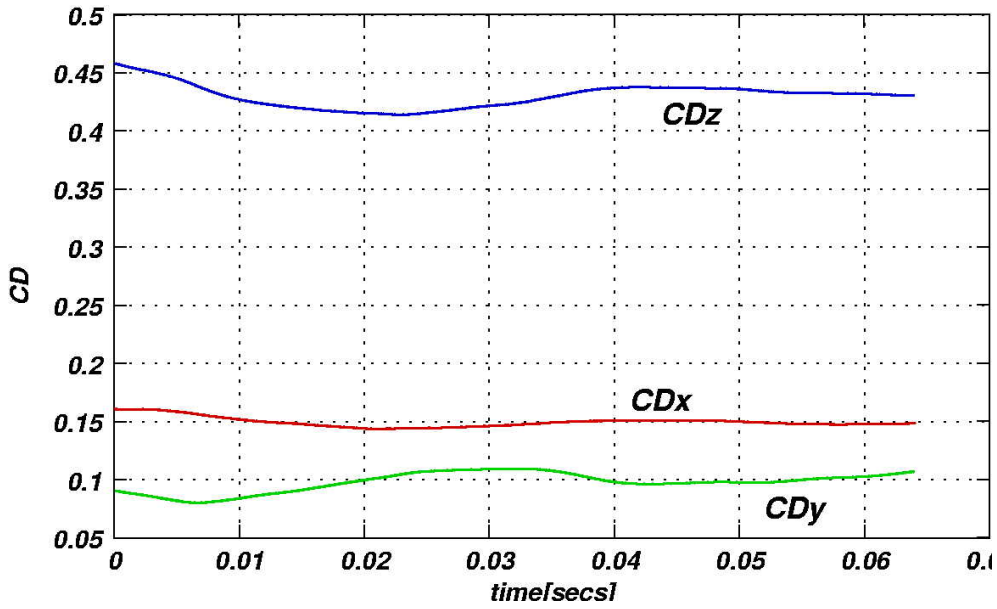

Figure 10: Drag coefficients for 5° of attack angle.

7 Conclusions

Large Eddy Simulations of the unsteady flow around a spinning projectile model were performed. The flow around this body is dominated by large coherent macro structures formed by a massive flow separation on the rear end. There was also a good agreement between the experimental and numerical predictions, evidenced by the similarity between the drag coefficient determined experimentally and numerically for the studied range of parameters. Finally, it is concluded that, according to the available computational resources, LES may be used as a feasible turbulence model for projectile aerodynamics.

Acknowledgments

This work was performed with the Free Software Foundation GNU-Project resources as Linux OS and Octave, as well another Open Source resources as PETSc, MPICH and OpenDX, and supported through grants CONICET PIP-02552/2000, ANPCyT FONCyT (PME-209 Cluster, PID 99-74 Flags), ANPCyT PICT-6973-BID-1201-OC-AR Proa and CAI+D-UNL-2000-43. The first author is Mechanical Engineer and Technical Division Chief of the CITEFA Weapons Systems Department. The support and grant of time given by the Technology and Innovation Management Office of CITEFA is also acknowledged.

References

[1] Silton, S. I., 2002. Navier-Stokes computations for a spinning projectile from subsonic to supersonic speeds. Tech. Rep. ARL-TR-2850, Army Research Laboratory.

[2] Sahu, J., 1991. Transonic Navier-Stokes computations for a spinning body of revolution. Tech. Rep. ARL-TR-3265, U.S. Army Research Laboratory.

[3] Weinacht, P., 2003. Prediction of projectile performance, stability, and free-flight motion using computational fluid dynamics. Tech. Rep. ARL-TR-3015, Army Research Laboratory.

[4] Townsend, A. A., 1980. *The structure of turbulent shear flow*, 2 ed. Cambridge Univ. Press, March.

[5] Rodi, W., 2006. "DNS and LES for some engineering flows". *Fluid Dynamics Research,* **38**, pp. 145–173.

[6] Sagaut, P., 2001. *Large eddy simulation for incompressible flows, an introduction.* Springer, Berlín.

[7] McDonough, J., 1995. "On intrinsic errors in turbulence models based on Reynolds-Averaged Navier-Stokes equations". *Int. J. Fluid Mech. Res.,* **22**, pp. 27–55.

[8] Wilcox, D., 1998. *Turbulence Modeling for CFD*, 2nd ed. DCW. ISBN: 0963605151.

[9] Calo, V., 2005. "Residual-based multiscale turbulence modeling: finite volume simulations of bypass transition". PhD thesis, Stanford University.

[10] Sahu, J., Heavey, K., Pressel, D., and Dinavahi, S., 1999. Parallel numerical computations of projectile flow fields. Tech. Rep. ARL-TR-2019, U.S. Army Research Laboratory.

[11] Sahu, J., and Heavey, K. R., 2004. "Advanced computational fluid dynamics simulations of projectiles with flow control". In Proceedings of SC2004 High Performance Computing, Networking and Storage Conference.

[12] Ray, S. E., and Tezduyar, T. E., 2000. "Fluid-object interactions in interior ballistics". *Computer Methods in Applied Mechanics and Engineering,* **19**, pp. 263–372.

[13] Sonzogni, V., Yommi, A., Nigro, N., and Storti, M., 2002. "A parallel finite element program on a Beowulf Cluster". *Advances in Engineering Software,* **33**, pp. 427–443.

[14] PETSc-FEM, 2007. A general purpose, parallel, multi-physics FEM program, GNU General Public License, http://www.cimec.ceride.gov.ar/petscfem.

[15] Message Passing Interface (MPI), 2007. http://www.mpi-forum.org/docs/docs.html.

[16] Balay, S., Gropp, W., McInnes, L., and Smith, B., 1997. Petsc 2.0 users manual. Tech. Rep. UC-405, Argonne Nat. Lab.

[17] Balay, S., Buschelman, K., Eijkhout, V., Gropp, W., Kaushik, D., Knepley, M., McInnes, L., Smith, B., and Zhang, H., 2005. Petsc 2.3.0 users manual. Tech. Rep. UC-405, Argonne Nat. Lab.

[18] Garibaldi, J., 2005. "Estudio del coeficiente de arrastre de un proyectil en flujo subsónico mediante una resolución de las ecuaciones de Navier-Stokes con cálculo paralelo". Master's thesis, Centro Internacional de Métodos Numéricos en Ingeniería (CIMNE), Universidad Politécnica de Barcelona (UPC), Barcelona.

[19] Hughes, T., and Brooks, A., 1979. "A multi-dimensional upwind scheme with no crosswind diffusion". In *Finite Element Methods for Convection Dominated Flows*, ASME, ed., Vol. 34. AMD, New York, pp. 19–35.

[20] Brooks, A., and Hughes, T., 1982. "Streamline upwind/Petrov-Galerkin formulations for convection dominated flows with particular emphasis on the incompressible Navier-Stokes equations". *Comp. Meth. App. Mech. Engng.,* **32**, pp. 199–259.

[21] Tezduyar, T., 1992. "Stabilized finite element formulations for incompressible flow computations". *Advances in Applied Mechanics,* **28**, pp. 1–44.

[22] Tezduyar, T., Mittal, S., Ray, S., and Shih, R., 1992. "Incompressible flow computations with stabilized bilinear and linear equal order interpolation velocity-pressure elements". *Comp. Meth. App. Mech. Engng.,* **95**, pp. 221–242.

[23] Smagorinsky, J., 1963. "General circulation experiments with the primitive equations: I. the basic equations". *Mon. Weather Rev.,* **91**, pp. 99–164.

[24] Paz, R., and Storti, M., 2005. "An interface strip preconditioner for domain decomposition methods. application to hydrology". *Int. J. for Num. Meth. in Engng.,* **62**(13), pp. 1873–1894.

[25] D'Elía, J., Storti, M., Oñate, E., and Idelsohn, S., 2002. "A nonlinear panel method in the time domain for seakeeping flow problems". *Int. J. of Computational Fluid Dynamics,* **16**(4), pp. 263–275.

[26] D'Elía, J., Storti, M., and Idelsohn, S., 2000. "A panel-Fourier method for free surface methods". *ASME-J. of Fluids Engng.,* **122**(2), June, pp. 309–317.

[27] Storti, M., and D'Elía, J., 2005. "Added mass of an oscillating hemisphere at very-low and very-high frequencies". *ASME-J. of Fluids Engng.,* **126**(6), November, pp. 1048–1053.

[28] Beowulf. The Beowulf Project, http://www.beowulf.org.

[29] The Geronimo cluster at cimec. http://www.cimec.org.ar/geronimo.

[30] Calise, A. J., and El-Shirbiny, H. A., 2001. "An analysis of aerodynamic control for direct fire spinning projectiles". In Guidance, Navigation and Control Conference, 2001, AIAA.

[31] Chen, Y., 1997. "High-order iterative learning control: Convergence, robustness and applications.". PhD thesis, Electrical & Electronic Engineering, Nanyang Technological University.

[32] Calvo, N., 2005. "Generación de mallas tridimensionales por métodos duales". PhD thesis, Facultad de Ingeniería y Ciencias Hídricas, Universidad Nacional del Litoral.